

Article

Recovery of Scratch Grooves in Ti-6Al-4V Alloy Caused by Reversible Phase Transformations

Artur R. Shugurov ^{1,*}, Alexey V. Panin ^{1,2}, Andrey I. Dmitriev ^{1,3} and Anton Yu. Nikonov ^{1,3} ¹ ISPMS Institute of Strength Physics and Material Science SB RAS, Akademicheskii pr. 2/4,

634055 Tomsk, Russia; pav@ispms.ru (A.V.P.); dmitr@ispms.ru (A.I.D.); anickonoff@ispms.ru (A.Y.N.)

² TPU National Research Tomsk Polytechnic University, School of Nuclear Science & Engineering, Lenin av. 30, 634050 Tomsk, Russia³ TSU Tomsk State University, Department of Metal Physics, Lenin av. 36, 634050 Tomsk, Russia

* Correspondence: shugurov@ispms.ru; Tel.: +7-3822-286-823

Received: 18 September 2020; Accepted: 2 October 2020; Published: 5 October 2020



Abstract: The deformation behaviors of Ti-6Al-4V alloy samples with lamellar and bimodal microstructures under scratch testing were studied experimentally and using molecular dynamics simulation. It was found that the scratch depth in the sample with a bimodal microstructure was twice as shallow as that measured in the sample with a lamellar microstructure. This effect is attributed to the higher hardness of the sample with a bimodal microstructure and the larger amount of elastic recovery of scratch grooves in this sample. On the basis of the results of molecular dynamics simulation, a mechanism was proposed, which associates the recovery of the scratch grooves with the inhomogeneous vanadium distribution in the β -areas. The calculations showed that at a vanadium content typical for Ti-6Al-4V alloy, both the body-centered cubic (BCC) and hexagonal close-packed (HCP) structures can be more energetically favorable depending on the atomic volume. Therefore, compressive or tensile stresses induced by the indenter could facilitate $\beta \rightarrow \alpha$ and $\alpha \rightarrow \beta$ phase transformations, respectively, in the vanadium-depleted domains of the β -areas, which contribute to the recovery of the Ti-6Al-4V alloy subjected to scratching.

Keywords: Ti-6Al-4V; scratch testing; molecular dynamics; microstructure; phase transformations

1. Introduction

Due to the remarkable combination of high specific strength, strong resistance to creep, excellent corrosion resistance and low heat conductivity, titanium and its alloys have been extensively used in a wide range of applications in aerospace, biomedical, chemical, marine, automotive and many other industries [1]. In most applications, high-strength $\alpha + \beta$ two-phase titanium alloys composed of HCP- α phase and BCC- β phase are generally utilized, among which Ti-6Al-4V is the most widely used and commercially available alloy. However, the poor wear resistance of titanium alloys, including Ti-6Al-4V, is still the main shortcoming that restricts their application, particularly in areas involving friction and wear [2,3].

Classical theories of wear suppose that the wear resistance of materials under abrasive [4] and adhesive [5] wear conditions is primarily defined by their hardness, and harder materials are usually more wear-resistant. However, as early as in the middle of the last century an improvement of the wear resistance of materials was also attributed to an increase in their ultimate elastic strain, i.e., to an increase in the contribution of the elastic strain to the total strain [6]. Therefore, it is currently commonly believed that the combination of high hardness H with low Young's modulus E , i.e., high H/E ratio, provides a better wear resistance to materials [7,8].

Since the mechanical properties of materials are highly dependent on their microstructure, the obvious way to obtain a material with a high H/E ratio is the optimization of its microstructure by varying processing parameters. In the case of Ti-6Al-4V alloy, a large variety of microstructures, including lamellar, martensite and equiaxed globular microstructures, as well as bimodal (duplex) microstructures composed of equiaxed α grains and transformed β areas, can be obtained depending on the thermomechanical processing routes [9,10]. While the effect of the microstructure of Ti-6Al-4V alloy on its mechanical properties, including hardness and Young's modulus, has been extensively studied, there is a lack of information about the effect of the Ti-6Al-4V microstructure on its elastic recovery, which should be pronounced at high H/E ratios. At the same time, recent studies have indicated that elastic recovery substantially affects the ploughing of metals, which is the main mechanism of abrasive wear [11,12].

Scratch testing is a promising technique for gaining insight into the mechanisms underlying plastic ploughing and the elastic recovery of metals. This technique makes it possible to study the deformation of multiphase materials, taking into account local features of their microstructure, i.e., to investigate the deformation of grains with different crystallographic orientations [13,14], to demonstrate the effects of internal interfaces [15,16], individual phases and inclusions [14,17] on deformation behavior, as well as to reveal the development of deformation phase transformations in the materials [18,19]. In addition to the experimental studies, molecular dynamics (MD) simulation is widely used for the investigation of nucleation and the development of plastic deformation in materials subjected to scratch testing. In particular, defect-free single crystals with face-centered cubic (FCC) [20–22] and BCC [23,24] crystal lattices were the focus of MD simulation of scratching. Alhafez et al. [25] used MD simulation to study the defect generation and plasticity in HCP crystals, with the basal and prismatic planes as the surfaces subjected to scratching by a hard tip. The authors' MD simulation showed that in the course of the scratching of Ti crystals, there is extensive defect-generation in the surface layers of the materials that is followed by the formation of disordered nanodomains [16,26]. The improvement of computer performance has promoted MD simulations of scratch testing of nanosized polycrystals [27,28], amorphous materials [29] and layered materials [30].

Despite a large amount of experimental and MD studies dealing with scratching different materials, there are only a few works considering the effect of the elastic recovery of a scratch groove on the mechanical and tribological properties of materials and mechanisms responsible for their enhanced recovery. Fan et al. [31] showed that the elastic recovery of fused silica under scratching has a significant effect on its hardness and friction coefficient. It has been supposed that reversible phase transformations could be responsible for the substantial recovery of scratch grooves in ultrasonically treated commercially pure titanium and Ti-6Al-4V [32]. More recently, it has been found that the development of direct and reverse $\alpha'' \rightarrow \alpha \rightarrow \alpha''$ martensitic transformations in the uppermost surface layer of Ti-6Al-4V samples subjected to low-energy, high-current pulsed electron beam treatment resulted in the enhancement of the elastic recovery of scratch grooves [33]. However, the effect of the microstructure of Ti-6Al-4V alloy on its ploughing behavior and elastic recovery has not been properly addressed. The objective of this work is to study, experimentally and using MD simulations, the mechanisms underlying the elastic recovery of scratch grooves in Ti-6Al-4V alloys with lamellar and bimodal microstructures.

2. Experimental Details

Two polycrystalline samples of Ti-6Al-4V alloy subjected to different processing routes were studied: a sample subjected to vacuum annealing for 2 h at a temperature of 980 °C (sample 1) and a sample obtained by hot compression at 950 °C with subsequent annealing at 900 °C for 1 h (sample 2). The rectangular samples $10 \times 10 \text{ mm}^2$ in size and 2 mm in height were cut from Ti-6Al-4V alloy billets. The samples were mechanically ground and subsequently electropolished to obtain smooth surfaces. The microstructure characterization of the samples was performed with an Axiovert 40 Mat optical microscope (Carl Zeiss, Göttingen, Germany). The phase compositions and structures of the coatings

were investigated using X-ray diffraction (XRD) with a Shimadzu XRD-7000 X-ray diffractometer (Shimadzu Corporation, Kyoto, Japan). The investigations were performed using $\text{CuK}\alpha$ radiation ($\lambda = 1.5406 \text{ \AA}$) in the Bragg–Brentano geometry. The measurements of the mechanical properties of the samples as well as their scratch testing were carried out using a NanoTest system (Micro Materials Ltd., Wrexham, UK). The nanoindentation measurements were performed in a load-controlled mode with a Berkovich diamond tip at a maximum load of 50 mN. The hardness H , the Young's modulus E and elastic recovery R were determined using the Oliver–Pharr method.

The scratch tests were performed using a conical diamond with a tip radius of $25 \mu\text{m}$. The scratching was carried out with a constant velocity of $10 \mu\text{m/s}$. Scratching tracks $600 \mu\text{m}$ long were applied to all samples. In the experiment, an initial surface profile of the tested samples was detected by pre-scanning with a very low load of $0.1 \mu\text{N}$ (no wear occurs at this load). During scratching, the surface profile could be sensed and recorded by the depth sensing system. After scratching, the surface profile of the samples was scanned again to record the deformation recovery. In the second step (scratching), the normal load applied to the indenter was sharply increased to maximum loads of 50, 100 and 200 mN, and maintained at a constant level thereafter. Five scratches were performed for each sample. After scratching, the surface topography of the samples in the vicinity of the scratch tracks was scanned using a Solver HV atomic force microscope (AFM, NT-MDT Co., Moscow, Russia) operating in a contact mode. A V-shaped silicon nitride cantilever (type SNL-10, Bruker Co., Berlin, Germany) was used with a nominal spring constant of 0.35 N/m and a tip radius of 12 nm . A series of 10 cross-sectional profiles of the scratch tracks were made and averaged to determine the residual scratch depth for each titanium sample.

3. Model Description

The model crystallite of HCP-Ti (α -phase) with the inclusion of BCC-Ti (β -phase) had the shape of a parallelepiped, with dimensions of $50 \times 26 \times 12 \text{ nm}$ along the X, Y and Z directions, respectively. The inclusion of BCC-Ti was modeled as an interlayer between two grains (grain 1 and grain 2) of HCP-Ti, as shown in Figure 1. The dimensions along the X axis were 20 nm for the grains and 10 nm for the inclusion. Taking into account the experimental data, the crystallographic orientations of the HCP grains along the X, Y and Z axes were chosen as $[\bar{1}6\bar{5}0]$, $[5\bar{2}3\bar{7}]$ and $[\bar{3}1\bar{2}2]$ (grain 1) and $[\bar{1}2\bar{3}2]$, $[3\bar{4}1\bar{3}]$ and $[3\bar{1}2\bar{2}]$ (grain 2), correspondingly. In the case of the inclusion of BCC-Ti, the $[100]$, $[010]$ and $[001]$ directions were oriented along the X, Y and Z axes, respectively. Two different Ti crystallites were studied to reveal the effect of vanadium, which is a stabilizer of the β -phase in Ti-6Al-4V alloy, on the mechanical behavior of the sample during scratching. In the first case, the inclusion of BCC-Ti contained 13 at. % of vanadium, which corresponds to a content of 4 wt. % in the model sample, which is typical for Ti-6Al-4V alloy. In the second case, a Ti crystallite with a vanadium-free inclusion was investigated. Thus, in both cases a Ti crystallite was modeled with incoherent boundaries between the grains and inclusion, for which the equilibrium configuration was obtained by the relaxation of the sample for 10 ns before scratching.

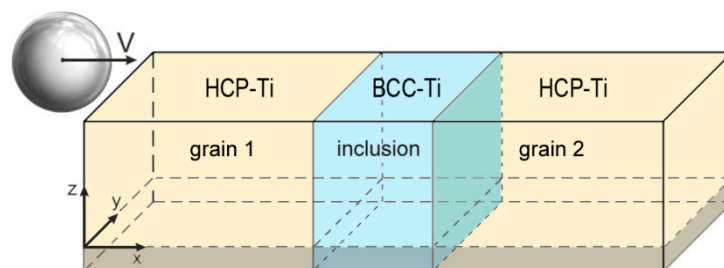


Figure 1. Molecular dynamic model of the scratch test for a HCP-Ti crystallite with inclusion of BCC-Ti.

The scratching was realized through the movement of a spherical indenter with a radius R of 6.5 nm. The indenter was moved along the X axis at a fixed depth of 3.5 nm and with a constant scratching speed of 15 m/s. Thus, atoms whose distance was less than the equilibrium radius R were acted upon by a force directed from the force center, equal to $F = -k(R - r)^2$, where k is the coefficient reflecting tip stiffness and r is the distance between the centers of the indenter and the atom. The coefficient k was chosen to be equal to $10 \text{ eV}/\text{\AA}^3$, similar to the earlier works [16,25,26]. The vertical immersion of the indenter into the crystallite was not considered. The lateral “incursion” of a previously immersed indenter on the initially defect-free crystallite was modeled, as shown in Figure 1. A 1.5 nm thick bottom layer (shown grey in Figure 1) simulated a fixed substrate, while other surfaces of the sample were considered free. The total number of atoms in the simulated crystallite exceeded one million. The interaction between Ti atoms was described by a potential [34] constructed using the embedded atom method. According to [34], this potential is suitable for the simulation of phase transitions and BCC-Ti. A potential obtained within the frame of the modified embedded atom method was used to describe the interaction between titanium and vanadium atoms [35]. The model sample was considered as an NVT ensemble that maintains the number of atoms N , the occupied volume V and the temperature of the system T . The initial temperature (100 K) of the simulation was achieved by using the velocity rescaling method during the MD simulation process from the balance between kinetic and thermal energies. The low temperature was used to avoid large thermal fluctuations, in order to provide a clear visualization of the structural defects. All MD calculations were implemented using the LAMMPS (large-scale atomic/molecular massively parallel simulator) molecular dynamics code [36]. To analyze the structure, the Dislocation Extraction Algorithm (DXA) and Common Neighbor Analysis (CNA) algorithms, implemented in the open visualization tool OVITO, were used [37]. The dislocation structure that evolved in HCP-Ti was analyzed only. The potential energy per atom in BCC and HCP Ti crystallites was calculated within the frame of the modified embedded atom method, using the following expression:

$$E = \frac{1}{N} \sum_i \left\{ F_i(\bar{\rho}_i) + \frac{1}{2} \sum_{i \neq j} \phi_{ij}(r_{ij}) \right\} \quad (1)$$

where F_i is the embedding function that represents the energy required to place atom i into the electron cloud, $\bar{\rho}_i$ is the electron charge density at the location of atom i , ϕ_{ij} is a pair-wise potential function, and r_{ij} is the distance between atoms i and j .

4. Experimental Results

The typical microstructures observed in the Ti-6Al-4V samples studied are shown in Figure 2. It is seen that sample 1 exhibits a fully lamellar morphology consisting of colonies of α -phase lamellae within large-body primary β -phase grains (Figure 2a). Sample 2 is characterized by a bimodal microstructure, which contains globular alpha grains and alpha/beta colonies (Figure 2b).

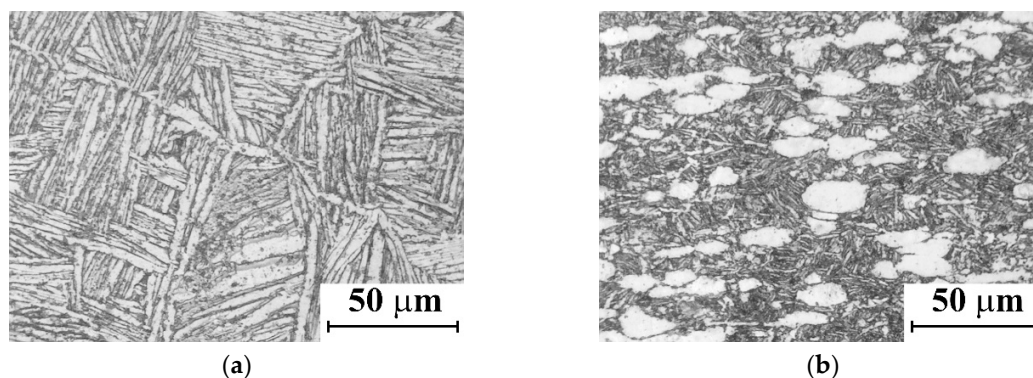


Figure 2. Lamellar (a) and bimodal (b) microstructures of Ti-6Al-4V alloy samples.

The XRD patterns of the samples primarily contain α -Ti peaks, which is typical for Ti-6Al-4V (Figure 3). The XRD pattern of sample 1 shows no preferred orientation of the α -phase (Figure 3, curve 1), while sample 2 demonstrates a pronounced crystallographic texture along the [002] direction (Figure 3, curve 2). In addition, the presence of small peaks of β -Ti phase is revealed in the XRD patterns, which indicates that there is a small amount of the β -phase retained in the final microstructure. It can be seen from Table 1 that the volume fraction of the β -phase in sample 2 is nearly 1.7 times lower than in sample 1. The lattice constants of the β -phase in samples 1 and 2 are 0.323 and 0.319 nm, respectively, which is less than the equilibrium value (0.332 nm). Since it is known that an increase in vanadium content results in decreasing the lattice constant of the β -phase in Ti-6Al-4V alloy [38], it can be inferred that the sample with a bimodal structure is characterized by higher vanadium content in the β -areas.

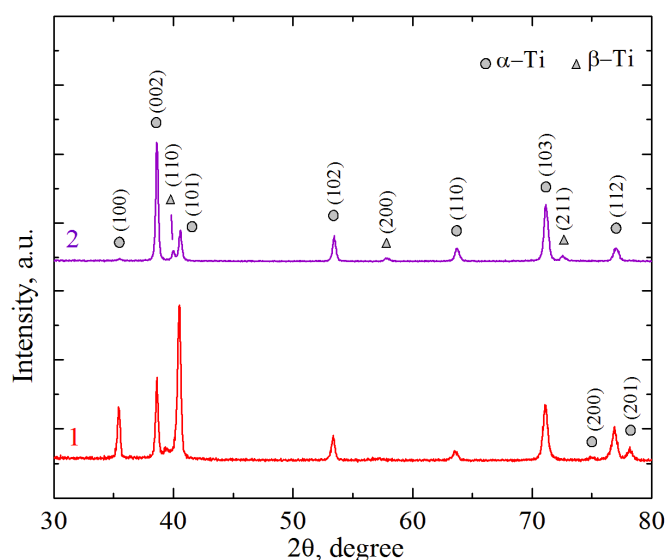


Figure 3. X-ray diffraction patterns of Ti-6Al-4V alloys with lamellar (1) and bimodal (2) microstructures.

The mechanical characteristics of the Ti-6Al-4V samples determined by instrumented indentation are listed in Table 1. It can be seen that sample 1 is characterized by a lower hardness than sample 2. In contrast, the Ti-6Al-4V sample with a bimodal microstructure has a lower Young's modulus. As a result, the H/E ratio and elastic recovery E_r are higher in sample 2 than in sample 1.

Table 1. Volume fraction of β -phase and mechanical properties of Ti-6Al-4V alloy samples.

Sample	Volume Fraction of β -phase, %	H , GPa	E , GPa	H/E	E_r , %
1	7.9	3.85 ± 0.42	154 ± 17	0.025	9
2	4.7	4.51 ± 0.44	146 ± 14	0.031	11

Scratch testing of the Ti-6Al-4V samples showed that they were subjected to ductile ploughing, which is a typical deformation mechanism for the scratching of metals. A combination of normal and tangential loads applied to the indenter resulted in the plastic edging of the material from the scratch grooves to their flanks, which led to the formation of pile-ups along the scratches (see Figure 4). It was found that deeper grooves form during scratching in sample 1, while the scratch grooves in sample 2 are rather shallow. The difference in the residual groove depths grows with increasing the applied load. As can be seen from the AFM images obtained in the vicinity of the scratch grooves and the corresponding surface profiles shown in Figure 4, the residual scratch depth at a load of 200 mN is close to 500 nm in sample 1, whereas it is less than half of this value in sample 2. The cross-sectional areas of the scratch grooves are 3.47 and 1.23 μm^2 , respectively. Moreover, a comparison of the longitudinal

surface profiles scanned before, during and after scratching shown in Figure 5 indicates that sample 2 is characterized not only by the smaller penetration depth of the indenter during scratching, but also by the higher recovery of the scratch groove. Indeed, while the groove in sample 1 is recovered after scratching, from ~ 800 to ~ 400 nm, i.e., by 50%, the groove recovery in sample 2 increases up to $\sim 65\%$ (from ~ 600 to ~ 200 nm). A large amount of elastic recovery of the material in sample 2 results in the formation of rather wide but shallow scratch grooves (see Figure 4d). As a result, the ratio of the cross-sectional area of the pile-ups at the groove flanks (1.02 and $0.68 \mu\text{m}^2$ in samples 1 and 2, respectively) to the cross-sectional area of the grooves increases from 0.29 (sample 1) to 0.55 (sample 2).

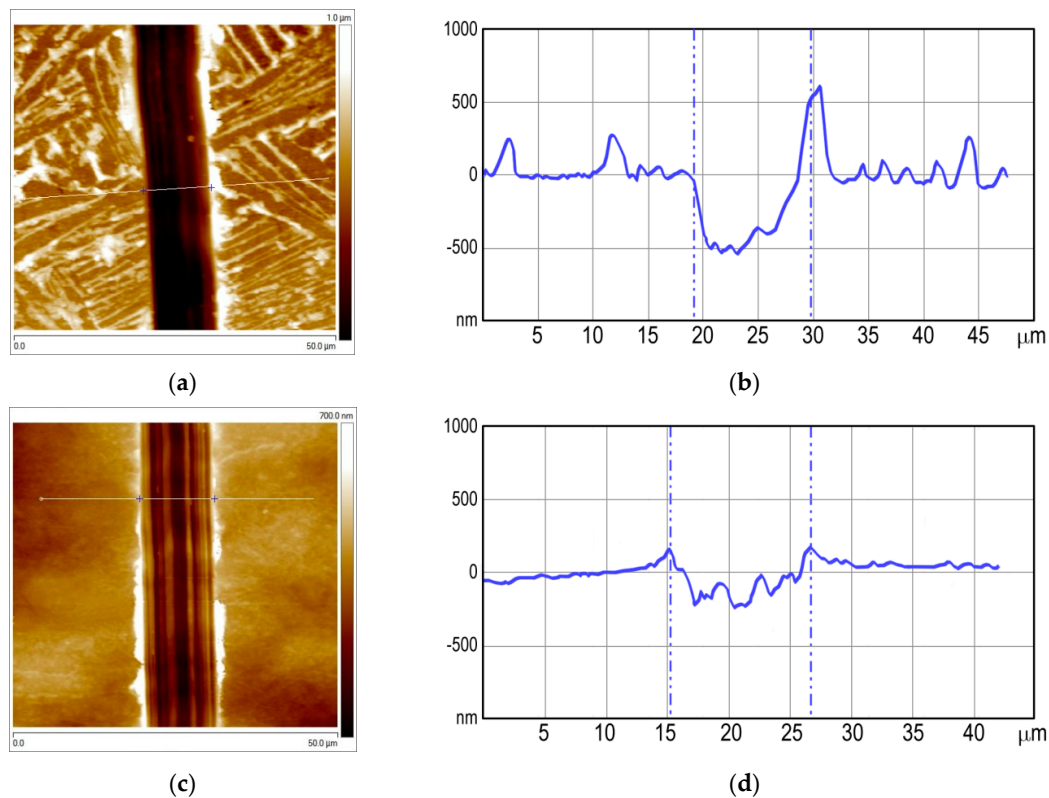


Figure 4. AFM images (a,c) and corresponding cross-sectional surface profiles (b,d) of scratch grooves formed at the applied load of 200 mN in Ti-6Al-4V alloy samples with lamellar (a,b) and bimodal (c,d) microstructures.

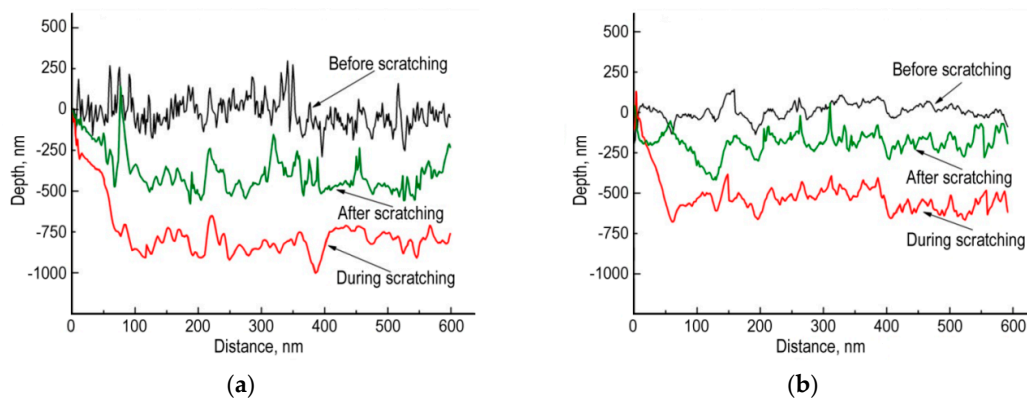


Figure 5. Surface profiles in Ti-6Al-4V samples 1 (a) and 2 (b) before, during and after scratching with an applied load of 200 mN.

The above described experiments revealed substantial difference in the elastic recovery of scratch grooves and imprints made by nanoindentation in the samples studied. The elastic recovery of the scratch grooves in the Ti-6Al-4V samples with lamellar and bimodal microstructures (50% and 65% respectively) is considerably higher than the recovery after nanoindentation (9% and 11%, correspondingly). Moreover, the difference between the E_r values for the samples reaches 15% in the case of scratching and drops to 2% for nanoindentation. These differences indicate that additional mechanisms of reversible deformation are activated upon the scratching of the Ti-6Al-4V alloy, which promotes material recovery under unloading. In particular, reversible deformation phase transformations can underlie this effect. Therefore, a molecular dynamics simulation of the evolution of the atomic structure in α -Ti crystallites with β -Ti inclusions during scratching was performed in order to gain a deeper insight into the development of reversible phase transformations in Ti-6Al-4V alloy.

5. Simulation Results

Figure 6 exhibits the evolution of the atomic structure in a Ti crystallite with a β -phase inclusion containing 13 at. % vanadium during scratching. Only BCC atoms are shown in Figure 6 in order to clearly visualize the observed changes in the atomic structure. Figure 6a,b correspond to the indenter positions in the middle of grain 1 and the BCC inclusion, respectively. A decrease in the inclusion volume, resulting from the rearrangement of a significant part of the BCC atoms into the HCP lattice of α -Ti, is clearly seen from the comparison of Figure 6a,b. After the indenter moved into grain 2, the BCC structure of the inclusion was largely recovered, as shown in Figure 6c.

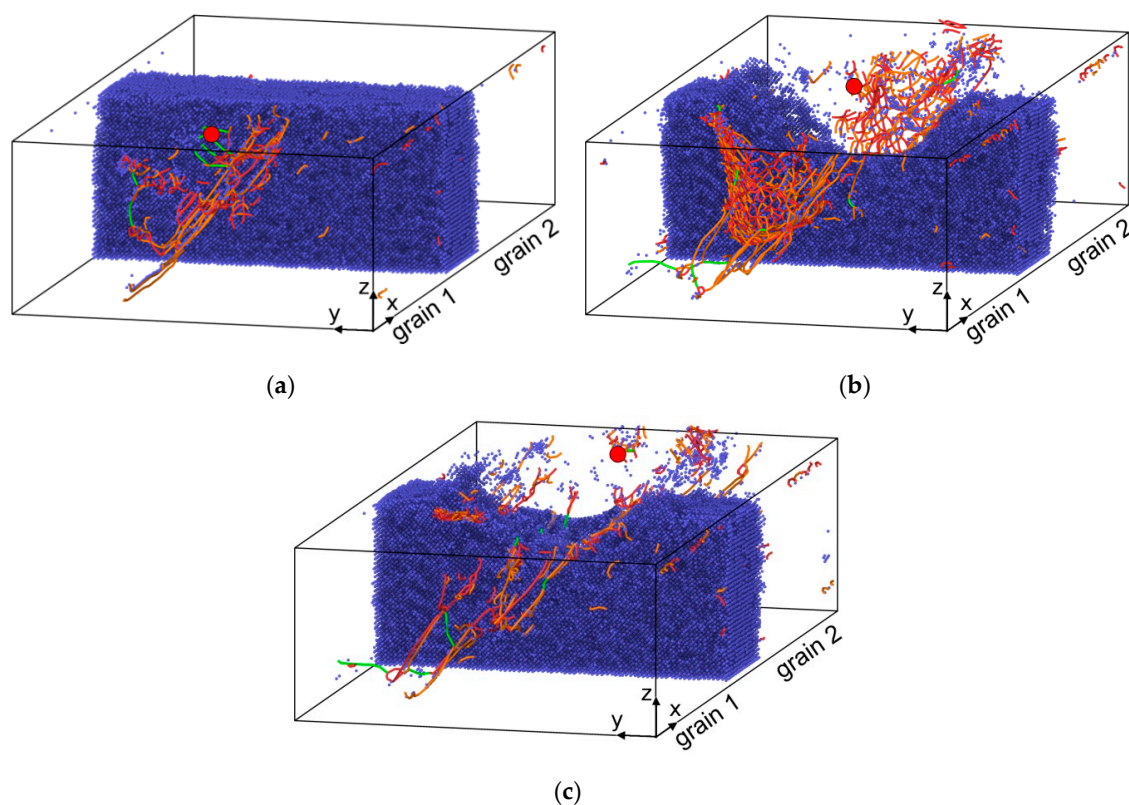


Figure 6. Snapshots displaying the structure of the model Ti crystallite with inclusion of β -Ti phase containing 13 at. % of vanadium after 10 (a) 25 (b) and 40 nm (c) of scratching. BCC atoms are shown as blue dots. Colored curves denote the dislocation core. Dislocations with the Burgers vectors $\mathbf{b}_1 = 1/3 \langle 1\bar{1}00 \rangle$ and $\mathbf{b}_2 = 1/3 \langle 1\bar{2}10 \rangle$ are shown in orange and green, respectively. Other dislocation lines are shown in red. Only the dislocations generated in HCP-Ti are shown. The large red dot marks the position of the indenter's center.

Figure 7 demonstrates the evolution of the volume fraction of BCC atoms in the β -Ti inclusions during scratching of the Ti crystallites. It is seen that in the case of the inclusion, where the BCC structure is stabilized by vanadium, the $\alpha \rightarrow \beta$ phase transformation leads to decreasing the fraction of BCC atoms down to ~ 0.7 (Figure 7, curve 1). The drop in the fraction of BCC atoms starts long before the indenter reaches the interphase boundary between grain 1 and the β -Ti inclusion. The minimum of the dependence corresponds to the point when the indenter is in the middle of the inclusion. A nearly full recovery of the fraction of BCC atoms is observed after scratching.

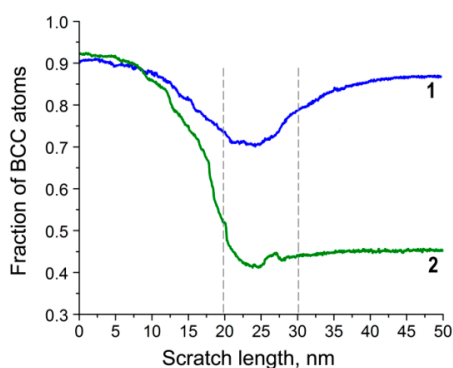


Figure 7. Volume fraction of BCC atoms in the β -Ti inclusion with 13 at. % of vanadium (curve 1) and the vanadium-free β -Ti inclusion (curve 2) as a function of the scratch length. Dashed lines indicate the boundaries of the inclusions.

The detailed studies of the evolution of atomic structure in the β -Ti inclusion containing 13 at. % of vanadium revealed that the development of phase transformations in the inclusion is concerned with its concentration inhomogeneity, i.e., non-uniform distribution of V atoms in the BCC lattice of titanium. Figure 8a exhibits the initial atomic structure of the analyzed fragment of the β -Ti inclusion (denoted as “A”), illustrating the configuration of the Ti and V atoms and the schematic showing the location of this fragment in the simulated crystallite. The dashed ovals in Figure 8a indicate the vanadium-enriched local regions (domains) of the fragment. Figure 8b–d demonstrate the evolution of the atomic structure of the fragment during scratching. CNA analysis was used to visualize atoms belonging to different local configurations of the crystal lattice. It is seen from the comparison of Figure 8a,b that the atomic rearrangement from the BCC lattice into the HCP lattice begins in the vanadium-depleted domains. In contrast, the vanadium-enriched domains largely maintain their BCC structure even when the indenter is in the middle part of the inclusion, which is accompanied by large lattice distortions (Figure 8c). The latter results in the formation of regions with a disordered atomic structure, the crystal lattice of which cannot be identified using CNA. Evidently, the atomic disorder depends on the arising of dislocations generated in the contact area of the indenter with the sample. When the indenter passes through the inclusion, the majority of the HCP atoms rearrange again into the BCC lattice, whereas the regions with a disordered lattice structure keep their structure (Figure 8d).

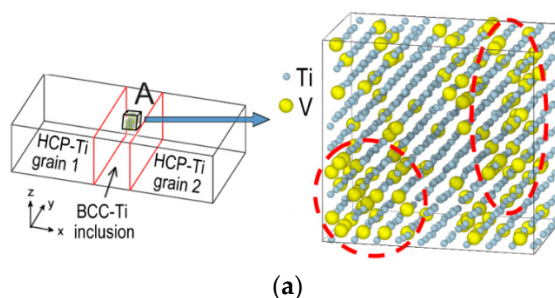


Figure 8. Cont.

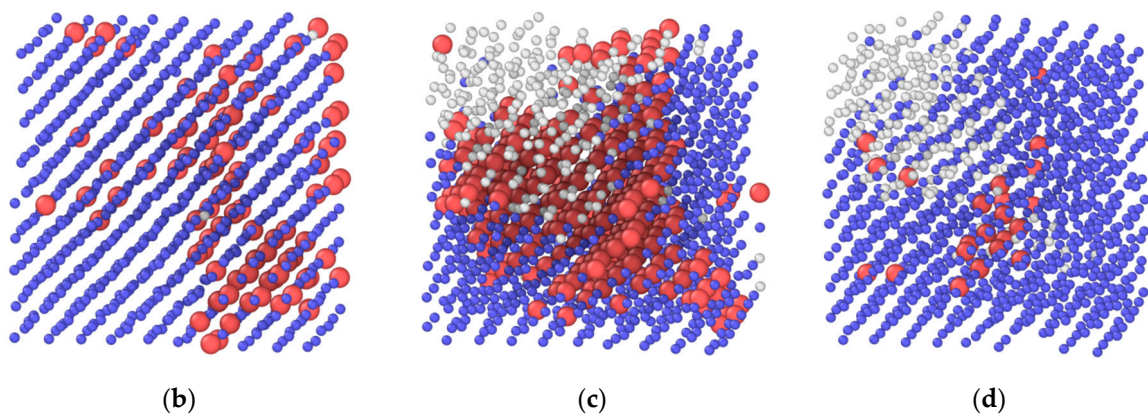


Figure 8. Location and atomic structure of fragment “A” in the β -Ti inclusion containing 13 at. % of vanadium (a). The dashed ovals indicate vanadium-enriched domains. Evolution of the atomic structure of the fragment at scratch lengths of 2 (b), 25 (c) and 35 nm (d). According to CNA [37], the HCP atoms are shown red, BCC atoms are shown in blue, and atoms belonging to unidentified lattice structures are shown in grey. For clarity, HCP atoms are shown as larger spheres.

Figure 9 shows the variation in the fractions of atoms with different local configurations of a crystal lattice in fragment “A” during scratching. It is seen that the decrease in the fraction of BCC atoms visible in Figure 7 is concerned with their rearrangement into the HCP configuration. The moving of the indenter into the β -Ti inclusion is accompanied by increasing the fraction of atoms the configuration of which is not identified because of strong lattice distortions and local atomic disordering. It should be noted that the increase in the fraction of the atoms with an unidentified lattice structure primarily occurs at the expense of decreasing the fraction of HCP atoms. After passing the indenter through the middle of the inclusion (at a scratch length of 25 nm), the restoration of the fraction of BCC atoms, and the corresponding reduction in the fractions of HCP atoms and atoms with unidentified lattice structures, are observed. Finally, when the indenter moves into grain 2, the fraction of HCP atoms in the studied fragment of the inclusion decreases by more than 90%, while the fraction of atoms with unidentified lattice structures decreases by only 20%. Thus, the restoration of the initial BCC structure primarily occurs by means of the reverse phase transformation of the HCP lattice formed under the influence of the indenter.

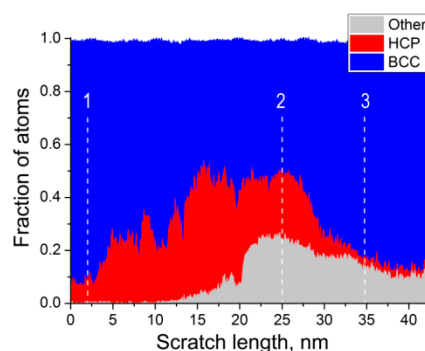


Figure 9. Fractions of atoms with different configurations of crystal lattice in fragment “A” of the β -Ti inclusion as a function of the scratch length. Vertical dashed lines 1, 2 and 3 mark positions of the indenter corresponding to the atomic structures shown in Figure 8b–d, respectively.

The key role of the domain structure of the β -Ti inclusions in the development of reverse $\alpha \rightarrow \beta$ phase transformations is clearly revealed in the simulation of scratching of a Ti crystallite with a vanadium-free BCC inclusion. As shown in Figure 10, in this case, a greater fraction of BCC atoms rearranges into the HCP lattice as compared with the inclusion containing vanadium (see Figure 6).

As a result, after passing the indenter through the vanadium-free β -Ti inclusion, the initial BCC structure maintains only in its bottom layers adjacent to the substrate with the rigidly fixed BCC lattice. It is also seen from Figure 7 (curve 2) that the minimum fraction of BCC atoms in the vanadium-free β -Ti inclusion drops to 0.4, and only slightly increases (up to 0.45) after passing the indenter.

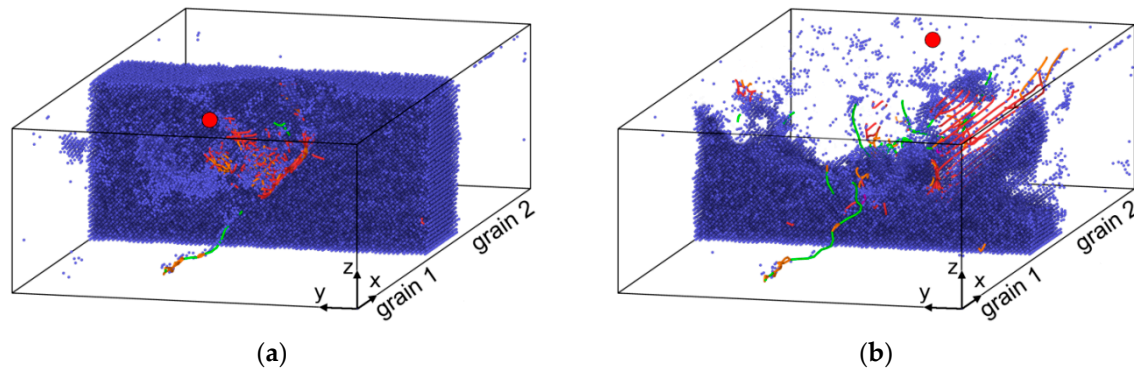


Figure 10. Snapshots displaying the resulting structure of the model Ti crystallite with the vanadium-free β -Ti inclusion after 10 (a) and 37 nm (b) of scratching. BCC atoms are shown as blue dots. Colored curves denote the dislocations cores. Dislocations with the Burgers vectors $\mathbf{b}_1 = \frac{1}{3} \langle 1\bar{1}00 \rangle$ and $\mathbf{b}_2 = \frac{1}{3} \langle 1\bar{2}10 \rangle$ are shown in orange and green, respectively. Other dislocation lines are shown in red. Only the dislocations generated in HCP-Ti are shown. The large red dot marks the position of the indenter.

6. Discussion

The results of scratch testing indicate that the Ti-6Al-4V sample with a bimodal microstructure is characterized by a substantially smaller residual scratch depth than the sample with a lamellar microstructure. This is in good agreement with the previous studies [10,38], which concluded that among the various morphologies, the bimodal microstructure possesses the best combination of strength and ductility. The origin of these improved mechanical properties is usually attributed to the fact that dislocation gliding inside the α -grains was blocked at the interfaces between them and the transformed β -areas, i.e., the β -areas with a finer morphology acted as a strengthening component for the mechanical properties of the bimodal microstructure [39]. On the other hand, recent studies argued that plastic strain can localize preferentially within the transformed β -areas, and then propagate into the surrounding α -grains [40]. Strain gradients from the interface to the interior of α -grains were supposed to increase the number of geometrically necessary dislocations near the interface, which contribute to the enhanced work-hardening rate of the bimodal microstructure. Evidently, both the mechanisms can contribute to the higher hardness of the Ti-6Al-4V sample with a bimodal microstructure, which results in the smaller penetration depth of the indenter during scratching. The mechanisms should become more pronounced with increasing the load applied to the indenter during scratching, because this results in the enlargement of the zone of local plastic strains and involves a greater number of interfaces between the α -grains and the β -areas in the deformation process. Therefore, the difference in the residual scratch groove depths in the samples with lamellar and bimodal microstructures grows with increasing the applied load.

Another origin of the smaller residual scratch depth in the sample with a bimodal microstructure is its higher recovery after scratching. This effect can be partially explained by increasing the contribution of elastic deformation to the total deformation of the material that is confirmed by the nanoindentation results, which demonstrate that the Ti-6Al-4V sample with a bimodal microstructure is characterized by higher values of H/E and E_r than the sample with a lamellar microstructure. However, the values of the recovery of the samples under scratching (15%) are substantially different from those under nanoindentation (2%). This indicates that, in contrast to the recovery of indenter imprints in the case of nanoindentation, the recovery of scratch grooves is caused not only by the elastic deformation of the Ti-6Al-4V samples, but also by the development of additional mechanisms of reversible deformation.

One of the mechanisms contributing to the formation and recovery of the scratch grooves is the reversible phase transformations developing during scratching. In particular, the enhanced elastic recovery of scratch grooves in Ti-6Al-4V samples subjected to electron beam treatment has been attributed to transformations of the more close-packed orthorhombic α'' -Ti phase into the HCP α -Ti phase, and vice versa [33]. The analysis of the total energy per atom, performed using MD calculations for Ti crystallites with BCC and HCP lattices, showed that the possibility of $\beta \leftrightarrow \alpha$ phase transformations substantially depends on the V content. Figure 11 shows the total energy per atom as a function of atomic volume in BCC and HCP Ti crystallites containing 5, 13 and 19 at. % of vanadium. It is seen from the Figure that at a low vanadium content (5 at. %), the HCP structure is more energetically favorable, while at the high content (19 at. %) the preferable configuration is BCC. At the same time, at the medium vanadium content (13 at. %), which is typical for the β -phase in Ti-6Al-4V alloy, the BCC and HCP structures are characterized by close values of the total energy. Therefore, in the latter case both the BCC and HCP structures can be more favorable, depending on the applied external load.

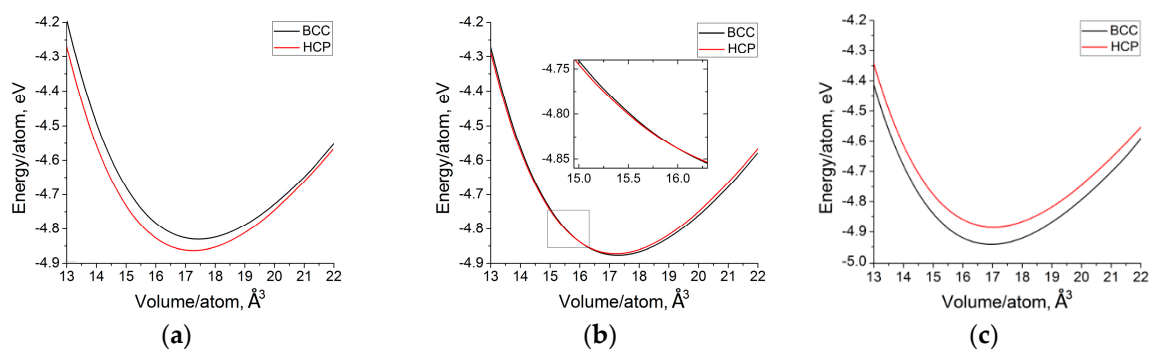


Figure 11. Energy per atom in the β -Ti inclusions with 5 (a), 13 (b) and 19 at. % of vanadium (c) as a function of atomic volume.

It has been shown that the indenter movement results in arising compressive stresses before and underneath it, as well as tensile stresses behind it [41]. Since the BCC β -phase of titanium is characterized by a lower packing density (0.68) than the HCP α -phase (0.74), it can be supposed that the compressive stresses arising ahead of and under the indenter facilitate the transformation of the β -phase into the more close-packed α -phase that results in deeper penetration of the indenter into the sample. It is clearly seen from Figure 11b that, although the minimum energy of the Ti crystallite with 13 at. % vanadium content in the β -phase, which lies in the range typical for Ti-6Al-4V alloy [42], corresponds to the BCC lattice, the HCP structure becomes more favorable with decreasing atomic volume.

The MD simulations showed that this $\beta \rightarrow \alpha$ phase transformation is possible only in the vanadium-depleted domains of the β -Ti inclusion, because vanadium is a β -phase stabilizer. Evidently, this effect should be more pronounced in the Ti-6Al-4V sample with lamellar microstructure, which is characterized by lower V content in the β -phase, and it is an additional factor that provides deeper scratch grooves in this sample (Figure 5a).

Phase transformations also contribute to the recovery of scratch grooves after scratching, which is substantially more pronounced in the sample with a bimodal microstructure. As can be seen from Figure 11b, with an increasing atomic volume, the BCC lattice structure becomes more favorable again in the Ti crystallite with a 13 at. % vanadium content. Therefore, when the indenter moves away, the relaxation of the compressive stresses and the arising of tensile stresses behind it favor the development of the reverse $\alpha \rightarrow \beta$ phase transformations in the vanadium-depleted domains of the β -Ti inclusion. This transformation behind the moving indenter allows a reduction in the energy of such domains, which are characterized by strong lattice distortions and, consequently, by high deformation energy. Moreover, the $\alpha \rightarrow \beta$ phase transformations in the HCP domains, surrounded by areas where the BCC lattice is stabilized by vanadium atoms, is accompanied by the annihilation of interphase boundaries

that also favors a reduction in the total energy of the Ti crystallites. Apparently, the dimensions of the vanadium-depleted domains should decrease with increasing V content in the β -Ti inclusions. The decrease in the domain size leads to the growth of the volume fraction of the boundaries between the HCP and BCC domains, and consequently, their annihilation contributes more to reducing the total energy of the β -Ti inclusions. Therefore, the recovery of scratch grooves is noticeably more pronounced in the Ti-6Al-4V sample with a bimodal microstructure, which is characterized by the higher vanadium content in the β -phase.

7. Conclusions

The investigation of Ti-6Al-4V alloys with lamellar and bimodal morphologies subjected to scratch testing revealed the strong dependence of scratch groove parameters (maximum and residual scratch depths, elastic recovery, volume of pile-up generated on the scratch flanks, etc.) on the microstructure. The bimodal microstructure was found to provide a scratch depth twice as shallow as that measured in the sample with a lamellar microstructure. This effect is assumed to be caused by the following: (i) the higher hardness of the Ti-6Al-4V sample with a bimodal microstructure resulting from the smaller grain size, and an enhanced work-hardening rate induced by the accumulation of dislocations at the interfaces between α -grains and β -areas; (ii) the greater degree of elastic recovery of scratch grooves in this sample due to the higher H/E ratio and the development of reversible $\beta \rightarrow \alpha \rightarrow \beta$ phase transformations in the β -areas.

According to the performed MD simulations, an important condition for the reversibility of the $\beta \rightarrow \alpha \rightarrow \beta$ phase transformations is the presence of vanadium in the BCC crystal lattice of titanium. The calculations showed that with a medium vanadium content in the β phase (13 at. %), both the BCC and HCP structures can be more energetically favorable, depending on the atomic volume. Therefore, compressive or tensile stresses induced by the indenter can facilitate direct $\beta \rightarrow \alpha$ or reverse $\alpha \rightarrow \beta$ phase transformations, respectively. In contrast, at low (5 at. %) and high (19 at. %) vanadium contents, the HCP and BCC structures, correspondingly, are more preferable regardless of the atomic volume. As a result, the lamellar microstructure, which is characterized by the larger volume fraction of the β -phase and, consequently, the lower V content in the β -areas, does not favor reverse $\alpha \rightarrow \beta$ phase transformations, which results in the lower recovery of the scratch grooves. The results obtained indicate the need to consider the effect of the microstructure of $\alpha + \beta$ titanium alloys on the ploughing mechanisms under abrasive wear, and can be useful for elaborating the methods to increase their abrasion resistance.

Author Contributions: Conceptualization, A.R.S. and A.I.D.; methodology, A.R.S.; software, A.I.D. and A.Y.N.; investigation, A.R.S., A.V.P. and A.Y.N.; writing—original draft preparation, A.R.S. and A.I.D.; writing—review and editing, A.R.S. and A.V.P.; visualization, A.Y.N.; project administration, A.R.S.; funding acquisition, A.R.S. All authors have read and agreed to the published version of the manuscript.

Funding: The work was performed according to the Government research assignment for ISPMS SB RAS, Projects III.23.1.1 and III.23.2.4. The authors also gratefully acknowledge the financial support granted by the Russian Foundation for Basic Research and the Government of the Tomsk region of the Russian Federation, grant № 18-48-700009.

Acknowledgments: The supercomputer of Tomsk State University was used in the framework of the TSU competitiveness improvement program.

Conflicts of Interest: The authors declare no conflict of interest.

References

1. Froes, F.H. *Titanium: Physical Metallurgy, Processing and Application*; ASM International: Materials Park, OH, USA, 2015.
2. Budinski, K.G. Tribological properties of titanium alloys. *Wear* **1991**, *151*, 203–217. [[CrossRef](#)]
3. Revankar, G.D.; Shetty, R.; Rao, S.S.; Gaitonde, V.N. Wear resistance enhancement of titanium alloy (Ti-6Al-4V) by ball burnishing process. *J. Mater. Res. Technol.* **2017**, *6*, 13–32. [[CrossRef](#)]

4. Rabinowicz, E. *Friction and Wear of Materials*; Wiley-Interscience: New York, NY, USA, 1965.
5. Archard, J.F. Contact and rubbing of flat surfaces. *J. Appl. Phys.* **1953**, *24*, 981–988. [[CrossRef](#)]
6. Oberle, T.L. Properties influencing wear of metals. *J. Metals.* **1951**, *3*, 438–439. [[CrossRef](#)]
7. Leyland, A.; Matthews, A. On the significance of the H/E ratio in wear control: A nanocomposite coating approach to optimised tribological behavior. *Wear* **2000**, *246*, 1–11. [[CrossRef](#)]
8. Attar, H.; Bermingham, M.J.; Ehtemam-Haghighi, S.; Dehghan-Manshadi, A.; Kent, D.; Dargusch, M.S. Evaluation of the mechanical and wear properties of titanium produced by three different additive manufacturing methods for biomedical application. *Mater. Sci. Eng. A* **2019**, *760*, 339–345. [[CrossRef](#)]
9. Lutjering, G. Influence of processing on microstructure and mechanical properties of ($\alpha+\beta$) titanium alloys. *Mater. Sci. Eng. A* **1998**, *243*, 32–45. [[CrossRef](#)]
10. Mironov, S.; Sato, Y.S.; Kokawa, H.; Hirano, S.; Pilchak, A.L.; Semiatin, S.L. Microstructural characterization of friction-stir processed Ti-6Al-4V. *Metals* **2020**, *10*, 976. [[CrossRef](#)]
11. Schibichski Kurelo, B.C.E.; de Oliveira, W.R.; Serbena, F.C.; de Souza, G.B. Surface mechanics and wear resistance of supermartensitic stainless steel nitrided by plasma immersion ion implantation. *Surf. Coat. Technol.* **2018**, *353*, 199–209. [[CrossRef](#)]
12. Tsybenko, H.; Xia, W.; Dehm, G.; Brinckmann, S. On the commensuration of plastic plowing at the microscale. *Tribol. Int.* **2020**, *151*, 106477. [[CrossRef](#)]
13. Shugurov, A.R.; Panin, A.V.; Dmitriev, A.I.; Nikonov, A.Y. The effect of the crystallographic grain orientation of polycrystalline Ti on plastic ploughing under scratch testing. *Wear* **2018**, *408–409*, 214–221. [[CrossRef](#)]
14. Kimm, J.; Sander, M.; Pöhl, F.; Theisen, W. Micromechanical characterization of hard phases by means of instrumented indentation and scratch testing. *Mater. Sci. Eng. A* **2019**, *768*, 138480. [[CrossRef](#)]
15. Machado, P.C.; Pereira, J.I.; Penagos, J.J.; Yonamine, T.; Sinatora, A. The effect of in-service work hardening and crystallographic orientation on the micro-scratch wear of Hadfield steel. *Wear* **2017**, *376*, 1064–1073. [[CrossRef](#)]
16. Dmitriev, A.I.; Nikonov, A.Y.; Shugurov, A.R.; Panin, A.V. The role of grain boundaries in rotational deformation in polycrystalline titanium under scratch testing. *Phys. Mesomech.* **2019**, *22*, 365–374. [[CrossRef](#)]
17. Liu, J.; Zeng, Q.; Xu, S. The state-of-art in characterizing the micro/nano-structure and mechanical properties of cement-based materials via scratch test. *Constr. Build. Mater.* **2020**, *254*, 119255. [[CrossRef](#)]
18. Chavoshi, S.Z.; Gallo, S.C.; Dong, H.; Luo, X. High temperature nanoscratching of single crystal silicon under reduced oxygen condition. *Mater. Sci. Eng. A* **2017**, *684*, 385–393. [[CrossRef](#)]
19. Wang, B.; Melkote, S.N.; Saraogi, S.; Wang, P. Effect of scratching speed on phase transformations in high-speed scratching of monocrystalline silicon. *Mater. Sci. Eng. A* **2020**, *772*, 138836. [[CrossRef](#)]
20. Zhang, P.; Zhao, H.; Shi, C.; Zhang, L.; Huang, H.; Ren, L. Influence of double-tip scratch and single-tip scratch on nano-scratching process via molecular dynamics simulation. *Appl. Surf. Sci.* **2013**, *280*, 751–756. [[CrossRef](#)]
21. Zhu, P.; Hu, Y.; Fang, F.; Wang, H. Multiscale simulations of nanoindentation and nanoscratch of single crystal copper. *Appl. Surf. Sci.* **2012**, *258*, 4624–4631. [[CrossRef](#)]
22. Ren, J.; Hao, M.; Lv, M.; Wang, S.; Zhu, B. Molecular dynamics research on ultra-high-speed grinding mechanism of monocrystalline nickel. *Appl. Surf. Sci.* **2018**, *455*, 629–634. [[CrossRef](#)]
23. Gao, Y.; Ruestes, C.J.; Urbassek, H.M. Nanoindentation and nanoscratching of iron: Atomistic simulation of dislocation generation and reactions. *Comput. Mater. Sci.* **2014**, *90*, 232–240. [[CrossRef](#)]
24. Wu, C.-D.; Fang, T.-H.; Lin, J.-F. Atomic-scale simulations of material behaviors and tribology properties for FCC and BCC metal films. *Mater. Lett.* **2012**, *80*, 59–62. [[CrossRef](#)]
25. Alabd Alhafez, I.; Urbassek, H.M. Scratching of hcp metals: A molecular-dynamics study. *Comput. Mater. Sci.* **2016**, *113*, 187–197. [[CrossRef](#)]
26. Dmitriev, A.I.; Nikonov, A.Y.; Shugurov, A.R.; Panin, A.V. Numerical study of atomic scale deformation mechanisms of Ti grains with different crystallographic orientation subjected to scratch testing. *Appl. Surf. Sci.* **2019**, *471*, 318–327. [[CrossRef](#)]
27. Liu, Y.; Li, B.; Kong, L. A molecular dynamics investigation into nanoscale scratching mechanism of polycrystalline silicon carbide. *Comput. Mater. Sci.* **2018**, *148*, 76–86. [[CrossRef](#)]
28. Gao, Y.; Urbassek, H.M. Scratching of nanocrystalline metals: A molecular dynamics study of Fe. *Appl. Surf. Sci.* **2016**, *389*, 688–695. [[CrossRef](#)]

29. Guo, X.; Zhai, C.; Kang, R.; Jin, Z. The mechanical properties of the scratched surface for silica glass by molecular dynamics simulation. *J. Non-Cryst. Solids*. **2015**, *420*, 1–6. [[CrossRef](#)]
30. Yang, W.; Ayoub, G.; Salehinia, I.; Mansoor, B.; Zbib, H. Multiaxial tension/compression asymmetry of Ti/TiN nano laminates: MD investigation. *Acta Mater.* **2017**, *135*, 348–360. [[CrossRef](#)]
31. Fan, X.; Li, C.; Sun, L.; Sun, H.; Jiang, Z. Hardness and friction coefficient of fused silica under scratching considering elastic recovery. *Ceram. Int.* **2020**, *46*, 8200–8208. [[CrossRef](#)]
32. Panin, V.E.; Panin, A.V.; Pochivalov, Y.I.; Elsukova, T.F.; Shugurov, A.R. Scale invariance of structural transformations in plastically deformed nanostructured solids. *Phys. Mesomech.* **2017**, *20*, 55–68. [[CrossRef](#)]
33. Sinyakova, E.A.; Panin, A.V.; Perevalova, O.B.; Shugurov, A.R.; Kalashnikov, M.P.; Teresov, A.D. The effect of phase transformations on the recovery of pulsed electron beam irradiated Ti-6Al-4V titanium alloy during scratching. *J. Alloys Compd.* **2019**, *795*, 275–283. [[CrossRef](#)]
34. Mendeleev, M.I.; Underwood, T.L.; Ackland, G.J. Development of an interatomic potential for the simulation of defects, plasticity, and phase transformations in titanium. *J. Chem. Phys.* **2016**, *145*, 154102. [[CrossRef](#)] [[PubMed](#)]
35. Maisel, S.B.; Ko, W.-S.; Zhang, J.-L.; Grabowski, B.; Neugebauer, J. Thermomechanical response of NiTi shape-memory nanoprecipitates in TiV alloys. *Phys. Rev. Mater.* **2017**, *1*, 033610. [[CrossRef](#)]
36. Plimpton, S. Fast Parallel Algorithms for Short-Range Molecular Dynamics. *J. Comput. Phys.* **1995**, *117*, 1–19. [[CrossRef](#)]
37. Stukowski, A.; Bulatov, V.V.; Arsenlis, A. Automated identification and indexing of dislocations in crystal interfaces. *Model. Simul. Mater. Sci. Eng.* **2012**, *20*, 085007. [[CrossRef](#)]
38. Elmer, J.W.; Palmer, T.A.; Babu, S.S.; Specht, E.D. In situ observations of lattice expansion and transformation rates of α and β phases in Ti-6Al-4V. *Mater. Sci. Eng. A* **2005**, *391*, 104–113. [[CrossRef](#)]
39. Bridier, F.; Villechaise, P.; Mendez, J. Slip and fatigue crack formation processes in an α/β titanium alloy in relation to crystallographic texture on different scales. *Acta Mater.* **2008**, *56*, 3951–3962. [[CrossRef](#)]
40. Chong, Y.; Bhattacharjee, T.; Park, M.-H.; Shibata, A.; Tsuji, N. Factors determining room temperature mechanical properties of bimodal microstructures in Ti-6Al-4V alloy. *Mater. Sci. Eng. A* **2018**, *730*, 217–222. [[CrossRef](#)]
41. Holmberg, K.; Laukkanen, A.; Ronkainen, H.; Wallin, K.; Varjus, S.; Koskinen, J. Tribological contact analysis of a rigid ball sliding on a hard coated surface Part I: Modelling stresses and strains. *Surf. Coat. Technol.* **2006**, *200*, 3793–3809. [[CrossRef](#)]
42. Lee, Y.T.; Welsch, G. Young's modulus and damping of Ti6Al4V alloy as a function of heat treatment and oxygen concentration. *Mater. Sci. Eng. A* **1990**, *128*, 77–89. [[CrossRef](#)]

